DOI: 10.24352/UB.OVGU-2017-051 TECHNISCHE MECHANIK, 34, 1, (2014), 23 – 38
submitted: November 4, 2013

Crystal Plasticity and Martensitic Transformations - A Phase Field Approach

R. Schmitt, C. Kuhn, R. Müller, K. Bhattacharya

A phase field model for martensitic transformations considering crystal plasticity effects is introduced. The evolution of microstructure is studied for two dimensions in detail, taking into account the transformation induced eigenstrain of the different martensitic orientation variants, as well as the activity on various slip systems of the different phases. With aid of the model, comprehensible numerical examples are evaluated, to understand the correlations of the different processes on the microscale. The numerical implementation is performed with finite elements. For the transient terms related to the evolution of microstructure, an implicit time integration scheme is applied on a global level, while for the crystal plasticity setting an implicit time integration scheme on the element level is employed.

1 Introduction

In manufacturing processes, surface hardening is often performed by thermal treatments. Cryogenic turning allows end shape machining and simultaneously attaining a hardened surface due to the martensitic transformation, (Skorupski et al. (2013a,b)). A longterm goal of this work is to contribute to a better understanding of the processes on the microscale induced by cryogenic turning.
During the martensitic transformation in austenitic steel, the atom lattice changes from the face centered cubic (fcc) phase to the body centered cubic (bcc) phase, i.e. the phase transition from austenite to martensite. The transformation of the atomic lattice leads to the transformation induced eigenstrain. Differing in their orientations to the austenitic lattice, there are several martensitic orientation variants with identical crystal structure, (Bhattacharya (2003)). This is depicted in Fig. 1 for a plane problem schematically. Additionally, the martensitic transforma-

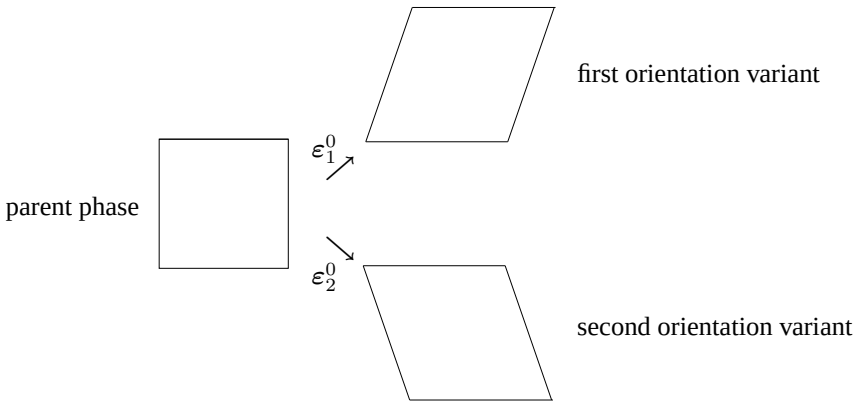

Figure 1: Orientation variants of the product phase.

tion is accompanied by dislocation movement which can be inherited by the martensitic phase and thus influences the microstructure evolution. To study these interactions, a continuum model for martenstitic transformations and plasticity is introduced in this work.
The continuum mechanics concerning phase transformations in solids can be found in Fischer et al. (1994). A micromechanical model for martensitic transformations is proposed by Bartel and Hackl (2008) and Bartel et al.

(2011), using the concept of energy relaxation, in combination with evolution equations derived from inelastic potentials. Cherkaoui and Berveiller (2000) assume in a conventional approach sharp interfaces between the different phases and model the martensitic transformation with the concept of moving boundaries. However, the tracking of those interfaces may become cumbersome. To circumvent these difficulties, an order parameter which regularizes discontinuities can be employed in the phase field approach. Based on Chen et al. (1992) and Wang and Khachaturyan (1997), there are several works, introducing the phase field method for martensitic transformations, e.g. Jin et al. (2001), Artemev et al. (2000), Kundin et al. (2011) which are based on fast Fourier transformation (FFT). Alternatively, finite differences (e.g. Yamanaka et al. (2008)) or finite elements (e.g. Hildebrand and Miehe (2011), Levitas et al. (2009)) are applied to solve the field equations. Equally there is literature, where crystal plasticity is considered for a phase field model for martensitic transformations. For example Yamanaka et al. (2009) examine with aid of a 3D model the growth of precipitates in elastoplastic materials. Hildebrand and Miehe (2012) apply finite gradient crystal plasticity for a variational phase field model, which focuses on the formation of plastic laminate deformation microstructure. In another work, Richards et al. (2013) study the complex correlations between the martensitic transformation and plastic slip for shape memory alloys on the mesoscale, employing FFT.
In this work an idealized problem motivated by microstructure evolution of steel is analysed, focussing on the impact of the transformation strain on the activation of different slip systems, and vice versa. The goal of this work is to model these interactions. Therefore, some basic examples are studied in detail.
The model introduced here is based on the phase field model for martensitic transformations proposed in Schmitt et al. (2013a) and Schmitt et al. (2013c). It considers the transformation induced eigenstrain, as a function of the order parameter. For this work, dislocation movement during the phase transformation is taken into account in the framework of crystal plasticity, using distinctive slip systems for the austenitic and the martensitic phase. Differing from the former ansatz, for the present approach a three well function is used to model the metastable and stable states of the system so that two martensitic orientation variants can be considered using a single order parameter. The idealized setting of two variants is reasonable since the model is limited to 2D. For the numerical realization, a finite element scheme is employed. It is noted that plasticity and phase transformation can interact in two ways - through kinetics and through the driving force, i.e. through the stresses. The former is well-studied in the literature (e.g. Olson and Cohen (1975)). However, the latter is also important but often overlooked. Therefore, in this work, the first is explicitly turned off to isolate the interactions through the stresses. This can easily be generalized.
The continuum phase field model for crystal plasticity and martensitic transformations is introduced in section 2. In section 3, the numerical realization is explained, considering the two different time scales of the model. The numerical results are examined in section 4, while basic examples are chosen to gain a better understanding for the correlations between the different processes on the microstructure. In the last section the main results and methods are summarized which finally leads to some comments referring to future work.

2 Continuum Phase Field Model Combining Crystal Plasticity and Martensitic Transformations

In this section, the continuum phase field model for crystal plasticity and martensitic transformations is developed, starting with the kinematics in subsection 2.1. The constitutive equations and evolution laws are given in subsection 2.2.

2.1 Kinematics

The total strain tensor $\boldsymbol{\varepsilon} = \nabla^{\text{sym}} \boldsymbol{u}$ is split up into the elastic strain $\boldsymbol{\varepsilon}^{\text{e}}$, the transformation induced eigenstrain $\boldsymbol{\varepsilon}^{0}$ and the plastic strain $\boldsymbol{\varepsilon}^{\text{p}}$,

$$\boldsymbol{\varepsilon} = \boldsymbol{\varepsilon}^{\text{e}} + \boldsymbol{\varepsilon}^{0} + \boldsymbol{\varepsilon}^{\text{p}}. \tag{1}$$

The global plastic strain $\boldsymbol{\varepsilon}^{\text{p}}$ is calculated from the slip γ_k in the k^{th} slip system,

$$\boldsymbol{\varepsilon}^{\text{p}} = \sum_{k=1}^{N} \gamma_k \, \boldsymbol{P}_k, \qquad \boldsymbol{P}_k = \frac{1}{2} \left[\boldsymbol{s}_k \otimes \boldsymbol{n}_k + \boldsymbol{n}_k \otimes \boldsymbol{s}_k \right], \tag{2}$$

where $\boldsymbol{s}_k$ is the slip direction and $\boldsymbol{n}_k$ the normal of the k^{th} slip system. In (2), the projector $\boldsymbol{P}_k$ is the strain (direction) associated with the k^{th} slip system, see for example Richards et al. (2013). For the 2D analysis in this work, two slip systems are considered for the austenitic phase ($k = 1, 2$) and the martensitic phases ($k = 3, 4$), respectively. These slip systems are identical in pairs, slip system $k=1$ corresponds to $k=3$ and $k=2$ corresponds to $k=4$.
In the phase field model the phase is indicated by an order parameter: Here $c = 0$ for the austenitic phase, and

$c=\pm 1$ for the two martensitic phases, the first ($c=1$) and the second ($c=-1$) martensitic orientation variant. Depending on the order parameter c, the elastic energy $W(\boldsymbol{\varepsilon}, c)$ is defined as

$$W(\boldsymbol{\varepsilon}, c) = \frac{1}{2}\left(\boldsymbol{\varepsilon} - \boldsymbol{\varepsilon}^0(c) - \boldsymbol{\varepsilon}^{\mathrm{p}}\right) : \left[\mathbb{C}(c)\left(\boldsymbol{\varepsilon} - \boldsymbol{\varepsilon}^0(c) - \boldsymbol{\varepsilon}^{\mathrm{p}}\right)\right]. \tag{3}$$

The eigenstrain tensor $\boldsymbol{\varepsilon}^0(c)$ is taken into account in a way that it considers the transformation shear ε^0_{12} on the off-diagonal entries and a volumetric transformation strain $\varepsilon^0_{\mathrm{vol}}$ on the diagonal entries. For the eigenstrain tensor $\boldsymbol{\varepsilon}^0(c)$ under plane strain conditions and the elasticity tensor $\mathbb{C}(c)$ the following dependencies on the order parameter c are assumed

$$\boldsymbol{\varepsilon}^0(c) = \begin{bmatrix} c^2\,\varepsilon^0_{\mathrm{vol}} & c\,\varepsilon^0_{12} \\ c\,\varepsilon^0_{12} & c^2\,\varepsilon^0_{\mathrm{vol}} \end{bmatrix}, \qquad \mathbb{C}(c) = \mathbb{C}_{\mathrm{fcc}} + c^2\left(\mathbb{C}_{\mathrm{bcc}} - \mathbb{C}_{\mathrm{fcc}}\right). \tag{4}$$

In order to consider for both orientation variants the same volumetric transformation strain $\varepsilon^0_{\mathrm{vol}}$ and the same elasticity tensor $\mathbb{C}_{\mathrm{bcc}}$, the dependence on the order parameter for these quantities is quadratic. The transformation shear changes sign for the different orientation variants and therefore dependes linearly on the order parameter.

2.2 Energetic Setting and Constitutive Laws

The local energy density ψ considered for this model consists of four parts, the elastic energy density W, the isotropic hardening potential W^{h}, the gradient energy density ψ^{grad} and the separation potential ψ^{sep},

$$\begin{aligned}\psi(\boldsymbol{\varepsilon}, c, \boldsymbol{\nabla} c, \gamma_k, \alpha_k) &= W(\boldsymbol{\varepsilon}^{\mathrm{e}}, c) + W^{\mathrm{h}}(\alpha_k) + \psi^{\mathrm{grad}}(\boldsymbol{\nabla} c) + \psi^{\mathrm{sep}}(c) \\ &= W(\boldsymbol{\varepsilon}^{\mathrm{e}}, c) + W^{\mathrm{h}}(\alpha_k) + \frac{1}{2}\kappa_{\mathrm{g}} G\, L ||\boldsymbol{\nabla} c||^2 + \kappa_{\mathrm{s}}\frac{G}{L} f(c),\end{aligned} \tag{5}$$

where α_k is the hardening variable of the k^{th} slip system. Based on Cahn and Hilliard (1958), in Schrade et al. (2008, 2013), the calculation of the calibration constants κ_{g} and κ_{s} is derived, which results in G corresponding to the free interface energy density, while the parameter L controls the width of the transition zone. The function $f(c)$ which appears in the separation potential ψ^{sep} is a Landau polynomial expansion, see Roumi (2010),

$$f(c) = \frac{(3\,A^2 - 1 - 2\,c^2)(1 - c^2)^2}{3\,A^2 - 1}, \tag{6}$$

where the coefficient A determines the height of the energy barrier. The plot of $f(c)$ in Figure 2 shows that the

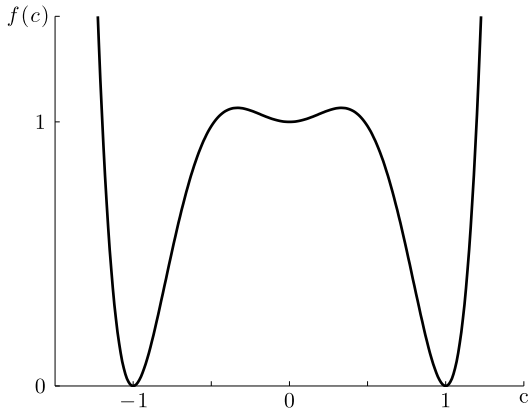

Figure 2: Landau polynomial expansion $f(c)$

function has a local minimum where $f(c) = 1$ for $c = 0$ which corresponds to the metastable austenitic phase, and two global minima where $f(c) = 0$ for $c = \pm 1$ corresponding to the stable martensitic phases.
As the driving force for the phase transformation**,** the variational derivative of the local total free energy ψ with respect to the order parameter c

$$d_c = -\frac{\delta \psi}{\delta c} \tag{7}$$

is taken into account. Assuming linear dependence of the microstructure evolution - and thus the temporal evolution of the order parameter c - on the driving force leads to the time-dependent Ginzburg-Landau equation (TDGL)

$$\dot{c} = -M\frac{\delta \psi}{\delta c} = -M\left[\frac{\partial W}{\partial c} + G\left(\frac{\kappa_{\mathrm{s}}}{L}\frac{\partial f}{\partial c} - \kappa_{\mathrm{g}}\, L\, \boldsymbol{\Delta} c\right)\right], \tag{8}$$

where the mobility parameter M influences the velocity of the martensitic transformations. Ignoring inertia effects and in absence of body forces, the balance of linear momentum reduces to the equilibrium condition

$$\text{div}\boldsymbol{\sigma} = \mathbf{0}, \tag{9}$$

for the Cauchy stress tensor $\boldsymbol{\sigma}$, given by the constitutive relation

$$\boldsymbol{\sigma} = \frac{\partial \psi}{\partial \boldsymbol{\varepsilon}} = \mathbb{C}(c)\left(\boldsymbol{\varepsilon} - \boldsymbol{\varepsilon}^0 - \boldsymbol{\varepsilon}^{\mathrm{p}}\right). \tag{10}$$

The equations (8) and (9) complete the set of field equations, where the mechanical balance equation (9) is coupled to the evolution equation of the order parameter (8) through the constitutive relation (10).
The isotropic hardening potential**,** which is part of the local energy density ψ in (5)**,** is introduced by

$$W^{\mathrm{h}} = \frac{1}{2}\sum_{k=1}^{N} H_k\,\alpha_k^2 \tag{11}$$

with the hardening moduls H_k. The slip γ_k and the harding parameter α_k are implemented as internal variables. If the yield criterion

$$\phi_k = |\tau_k| - \tau_k^{\mathrm{cr}} > 0 \quad \text{with} \quad \tau_k^{\mathrm{cr}}(c) = d_k^{\mathrm{cr}}(c) + H_k\,\alpha_k, \tag{12}$$

is satisfied, the slip system becomes active. In an active slip system, the slip γ_k and the hardening α_k are assumed to evolve as follows

$$\dot{\gamma}_k = \frac{1}{\eta}\left\langle |\tau_k| - \tau_k^{\mathrm{cr}} \right\rangle \operatorname{sgn}(\tau_k), \qquad \dot{\alpha}_k = |\dot{\gamma}_k|, \tag{13}$$

where η is the viscosity coefficient, and the symbol $\langle\cdot\rangle$ represents the Macaulay brackets. With the help of the projector $\boldsymbol{P}_k$ the resolved shear is given by

$$\tau_k = \boldsymbol{P}_k : \boldsymbol{\sigma} = \boldsymbol{\sigma} : \boldsymbol{P}_k. \tag{14}$$

In (12)**,** the critical driving force for plasticity $d_k^{\mathrm{cr}}(c)$ depends on the order parameter c since only the slip systems of the present phase can be activated. For austenitic material ($c = 0$), the critical shear stress of the austenitic phase $\tau_{\mathrm{fcc}}^{\mathrm{cr}}$ is taken into account for the austenitic slip systems ($k = 1, 2$). The criticial shear stress of the martensitic phase $\tau_{\mathrm{bcc}}^{\mathrm{cr}}$ is set to a sufficiently high value for the martensitic slip systems ($k = 3, 4$), so that these remain inactive. Analogously, for $c = \pm 1$, $\tau_{\mathrm{bcc}}^{\mathrm{cr}}$ is taken into account for $k = 3, 4$ and $\tau_{\mathrm{fcc}}^{\mathrm{cr}}$ is set to a high value for $k = 1, 2$ by the following relation

$$d_k^{\mathrm{cr}}(c) = \begin{cases} k^{\infty}\left[\dfrac{\tau_{\mathrm{fcc}}^{\mathrm{cr}}}{k^{\infty}} + 1 + \tanh\left(k_1\,c - k_2\right) + 1 - \tanh\left(k_1\,c + k_2\right)\right] & k = 1, 2 \quad (c = 0) \\ k^{\infty}\left[\dfrac{\tau_{\mathrm{bcc}}^{\mathrm{cr}}}{k^{\infty}} + \tanh\left(k_1\,c + k_2\right) - \tanh\left(k_1\,c - k_2\right)\right] & k = 3, 4 \quad (c = \pm 1) \end{cases}. \tag{15}$$

Figure 3 shows the plot of the function $d_k^{\mathrm{cr}}(c)$, where the dotted line corresponds to the austenitic phase, i.e. for $c = 0$ the slip systems $k = 1, 2$ can be activated; the continuous line corresponds to the martensitic phase, where for $c = \pm 1$ the slip systems $k = 3, 4$ are available.

3 Numerical Procedures

The model is implemented in a 2D-FEM framework with the mechanical displacements $\boldsymbol{u}$ and the order parameter c as nodal degrees of freedom, considering two time scales. For the transient terms related to the evolution of the order parameter c, a backward Euler scheme is applied on the global level, solving for each time step the set of coupled field equations. The numerical realization is explained in subsection 3.1. To evaluate the evolution equations of the slip and the hardening, a backward Euler scheme is used on the element level, which is discussed in subsection 3.2.

3.1 Numerical Implementation: The Global Time Scale

On the global time scale the transient terms are discretized in time using the Euler backward time integration scheme. The numerical implementation is explained in detail in Schrade et al. (2007). The starting point are the

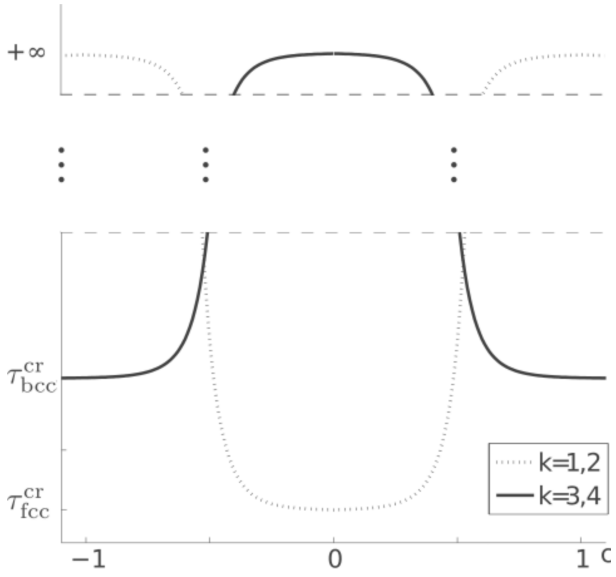

Figure 3: Critical driving force for plasticity $d_k^{\mathrm{cr}}(c)$

weak formulations of the field equations (8) and (9) using the test functions $\boldsymbol{\eta}_u$, η_c

$$\int_V \boldsymbol{\nabla}\boldsymbol{\eta}_u : \boldsymbol{\sigma}\,\mathrm{d}V = \int_{\partial V_t} \boldsymbol{\eta}_u \cdot \boldsymbol{t}^*\,\mathrm{d}A, \tag{16}$$

and

$$\int_V \eta_c \frac{\dot{c}}{M}\,\mathrm{d}V - \int_V \boldsymbol{\nabla}\eta_c\,\boldsymbol{q}\,\mathrm{d}V + \int_V \eta_c \left(\frac{\partial W}{\partial c} + G\,\frac{\kappa_{\mathrm{s}}}{L}\frac{\partial f}{\partial c}\right)\mathrm{d}V = -\int_{\partial V} \eta_c\, q^*\,\mathrm{d}A, \tag{17}$$

with $\boldsymbol{q} = -\,\kappa_{\mathrm{g}}\,G\,L\,\boldsymbol{\nabla}c$. The boundary conditions for the stresses $\boldsymbol{\sigma}$ is the traction $\boldsymbol{t}^* = \boldsymbol{\sigma}\boldsymbol{n}$ and for $\boldsymbol{q}$ the normal flux $q^* = \boldsymbol{q}\cdot\boldsymbol{n}$ with $q^* = 0$, where $\boldsymbol{n}$ is the outer normal vector to the volume V. The rate $\dot{c}$ is computed by a time discretization. If j denotes the time step t_j the difference formula

$$\dot{c} = \frac{c^{(j+1)} - c^{(j)}}{\Delta t}$$

is used.
Using the shape functions N_I for node I, the fields $\boldsymbol{u}$, $\boldsymbol{\varepsilon}$ and c, $\boldsymbol{\nabla}c$ and $\dot{c}$ are discretized with Voigt notation denoted by an underbar $\underline{(\cdot)}$:

$$\underline{\boldsymbol{u}} = \sum_{I=1}^{N} N_I\,\underline{\hat{\boldsymbol{u}}}_I, \qquad \underline{\boldsymbol{\varepsilon}} = \sum_{I=1}^{N} \underline{\boldsymbol{B}}_I^u\,\underline{\hat{\boldsymbol{u}}}_I, \tag{18}$$

$$c = \sum_{I=1}^{N} N_I\,\hat{c}_I, \qquad \underline{\nabla c} = \sum_{I=1}^{N} \underline{\boldsymbol{B}}_I^c\,\hat{c}_I, \tag{19}$$

$$\dot{c} = \sum_{I=1}^{N} N_I\ = \sum_{I=1}^{N} N_I\,\hat{\dot{c}}_I, \tag{20}$$

where

$$\underline{\boldsymbol{B}}_I^u = \begin{bmatrix} N_{I,x} & 0 \\ 0 & N_{I,y} \\ N_{I,y} & N_{I,x} \end{bmatrix} \quad \text{and} \quad \underline{\boldsymbol{B}}_I^c = \begin{bmatrix} N_{I,x} \\ N_{I,y} \end{bmatrix}. \tag{21}$$

The nodal quantities are denoted by the superimposed hat $\hat{(\cdot)}$. In a next step, these discretizations are applied to equations (16) and (17) to obtain the nodal residuals as a function of the nodal degrees of freedom $\hat{\underline{\boldsymbol{d}}}_J = (\underline{\hat{\boldsymbol{u}}}_J, \hat{c}_J)^T$

and the rates $\underline{\dot{\hat{d}}}_J$,

$$\underline{\boldsymbol{R}}_I\left(\underline{\hat{\boldsymbol{d}}}_J, \underline{\dot{\hat{d}}}_J\right) = \left[\begin{array}{c} \underline{\boldsymbol{R}}_I^u(\underline{\hat{\boldsymbol{d}}}_J) \\ R_I^c(\underline{\hat{\boldsymbol{d}}}_J, \underline{\dot{\hat{\boldsymbol{d}}}}_J) \end{array}\right] = \\ = \left[\begin{array}{c} \int\limits_V \left(\underline{\boldsymbol{B}}_I^u\right)^T \underline{\boldsymbol{\sigma}}\, \mathrm{d}V \\ \int\limits_V N_I \frac{\dot{c}}{M}\, \mathrm{d}V - \int\limits_V \underline{\boldsymbol{B}}_I^{cT} \boldsymbol{q}\, \mathrm{d}V + \int\limits_V N_I \left(\frac{\partial W}{\partial c} + G\,\frac{\kappa_\mathrm{s}}{L}\frac{\partial f}{\partial c}\right) \mathrm{d}V \end{array}\right]. \tag{22}$$

Note that in the derivation of (22) boundary tractions $\boldsymbol{t}^*$ and boundary fluxes q^* have been neglected. The derivative of the nodal residuals with respect to the nodal degrees of freedom yields the entries of the tangent matrix $\underline{\boldsymbol{K}}_{IJ}$ given by

$$\underline{\boldsymbol{K}}_{IJ} = \frac{\partial \underline{\boldsymbol{R}}_I}{\partial \underline{\hat{\boldsymbol{d}}}_J} = \left[\begin{array}{cc} \underline{\boldsymbol{K}}_{IJ}^{uu} & \underline{\boldsymbol{K}}_{IJ}^{uc} \\ \underline{\boldsymbol{K}}_{IJ}^{cu} & \underline{\boldsymbol{K}}_{IJ}^{cc} \end{array}\right], \tag{23}$$

with

$$\underline{\boldsymbol{K}}_{IJ}^{uu} = \int_V \left(\underline{\boldsymbol{B}}_I^u\right)^T \underline{\mathbb{C}}\, \underline{\boldsymbol{B}}_J^u\, \mathrm{d}V$$

$$\underline{\boldsymbol{K}}_{IJ}^{uc} = \underline{\boldsymbol{K}}_{IJ}^{cu} = \int_V \left(\underline{\boldsymbol{B}}_I^u\right)^T \left(\underline{\tilde{\boldsymbol{\sigma}}} - \underline{\boldsymbol{\sigma}}^0\right) N_J\, \mathrm{d}V$$

$$\underline{\boldsymbol{K}}_{IJ}^{cc} = \int_V \left(\kappa_\mathrm{g} G L\, \left(\underline{\boldsymbol{B}}_I^c\right)^T \underline{\boldsymbol{B}}_J^c + N_I \left(\left(\underline{\varepsilon}^0\right)^T \left(\underline{\boldsymbol{\sigma}}^0 - 2\underline{\tilde{\boldsymbol{\sigma}}}\right) + \kappa_\mathrm{s} \frac{G}{L}\frac{\partial^2 f}{\partial c^2}\right) N_J\right) \mathrm{d}V$$

where $\underline{\tilde{\boldsymbol{\sigma}}} = 2\,c\,(\underline{\mathbb{C}}_M - \underline{\mathbb{C}}_A)\left(\underline{\boldsymbol{\varepsilon}} - \underline{\boldsymbol{\varepsilon}}^0(c) - \underline{\boldsymbol{\varepsilon}}^\mathrm{p}\right)$ and $\underline{\boldsymbol{\sigma}}^0 = \underline{\mathbb{C}}(c)\,\dfrac{\partial \underline{\boldsymbol{\varepsilon}}^0(c)}{\partial c}$.
Furthermore, the damping matrix $\underline{\boldsymbol{D}}_{IJ}$ reads

$$\underline{\boldsymbol{D}}_{IJ} = \frac{\partial \underline{\boldsymbol{R}}_I}{\partial \underline{\dot{\hat{\boldsymbol{d}}}}_J} = \int\limits_V \left[\begin{array}{ccc} 0 & 0 & 0 \\ 0 & 0 & 0 \\ 0 & 0 & \frac{1}{M} N_I\, N_J \end{array}\right] \mathrm{d}V. \tag{24}$$

The integrals are evaluated using Gauß quadrature. With the knowledge of $\underline{\boldsymbol{K}}_{IJ}$ and $\underline{\boldsymbol{D}}_{IJ}$ the implicit time integration can be performed. This results in a system matrix $\underline{\boldsymbol{S}}_{IJ} = \dfrac{1}{\Delta t}\underline{\boldsymbol{D}}_{IJ} + \underline{\boldsymbol{K}}_{IJ}$ after time discretization. The matrix $\underline{\boldsymbol{S}}_{IJ}$ is used in a global Newton iteration to compute the increments of $\underline{\hat{d}}_J$ for the new time step $t^{(j+1)}$ (implicit scheme).

3.2 Local Time Discretization Algorithm

The algorithm for the time integration of the evolution equations of the crystal plasticity setting is also based on an implicit Euler backward scheme, in form of a predictor corrector method, where the time interval $[t^{(n)}, t^{(n+1)}]$ is considered. Furthermore, the variables at $t = t^{(n)}$ are known. In the first predictor step, an elastic trial value for the strains is given with $\underline{\boldsymbol{\varepsilon}}^{\mathrm{p,tr}} = \underline{\boldsymbol{\varepsilon}}^{\mathrm{p}(n)}$, so the resolved shear stress on all slip systems k can be calculated for the trial state

$$\underline{\boldsymbol{\sigma}}^{\mathrm{tr}} = \underline{\mathbb{C}}(c)\left(\underline{\boldsymbol{\varepsilon}} - \underline{\boldsymbol{\varepsilon}}^0(c) - \underline{\boldsymbol{\varepsilon}}^{\mathrm{p}(n)}\right), \tag{25}$$

$$\tau_k^{\mathrm{tr}} = \underline{\boldsymbol{\sigma}}^{\mathrm{tr}^T} \cdot \underline{\boldsymbol{P}}_k. \tag{26}$$

Subsequently, for each slip system k the yield criterion is checked by the trial state

$$\phi_k^{\mathrm{tr}} = |\tau_k^{\mathrm{tr}}| - \tau_k^{\mathrm{cr,tr}}(c), \tag{27}$$

where $\alpha_k^{\mathrm{tr}} = \alpha_k^{(n)}$. If $\phi_k^{\mathrm{tr}} > 0$, k is an active slip system. For active slip systems the update formula for

$$\gamma_k^{(n+1)} = \gamma_k^{(n)} + \Delta\gamma_k^{(n+1)}\ \mathrm{sgn}(\tau_k^{\mathrm{tr}}) \quad \text{with} \quad \Delta\gamma_k = \frac{\Delta t}{\eta}\,\phi_k^{(n+1)} \tag{28}$$

results from the time discretization of the evolution law (13). To obtain $\Delta\gamma_k^{(n+1)}$, the update formula for the yield function can be recast according to a similar procedure as in Schröder and Miehe (1997) in the format

$$\phi_k^{(n+1)} = \phi_k^{\text{tr}} - \sum_{l=1}^{N_{\text{act}}} (R_{kl} + H_{kl}\ \delta_{kl})\ \Delta\gamma_l, \tag{29}$$

where

$$R_{kl} = \underline{P}_k^T\ \underline{\mathbb{C}}(c)\ \underline{P}_l\ \text{sgn}({\tau_k}^{\text{tr}})\ \text{sgn}({\tau_l}^{\text{tr}}), \tag{30}$$

with the identity tensor δ_{kl}, and the diagonal matrix $H_{kl} = \text{diag}(H_k)$. Furthermore, $l \in \{1, ..., N^{\text{act}}\}$ denotes the l^{th} of N^{act} active slip systems. Together with the definition of $\Delta\gamma_k$ in (28), (29) forms a set of linear equations for the $\Delta\gamma_l$

$$\sum_{l=1}^{N_{\text{act}}} \underbrace{\left[\delta_{kl} + \frac{\Delta t}{\eta}\,(R_{kl} + H_{kl})\right]}_{A_{kl}} \Delta\gamma_l = \underbrace{\frac{\Delta t}{\eta}\ \phi_k^{\text{tr}}}_{b_k}. \tag{31}$$

Finally, the values for the stresses $\boldsymbol{\sigma}$ and the tangent moduli $\mathbb{C}(c)$ are computed for the time step $t = t^{(n+1)}$

$$\underline{\boldsymbol{\sigma}}^{(n+1)} = \underline{\mathbb{C}}(c)\left[\underline{\boldsymbol{\varepsilon}}^{(n+1)} - \sum_{k=1}^{N} \gamma_k^{(n+1)}\ \underline{\boldsymbol{P}}_k\right], \tag{32}$$

$$\underline{\mathbb{C}}^{\text{tan}(n+1)}(c) = \underline{\mathbb{C}}(c) - \sum_{k=1}^{N_{\text{act}}}\sum_{l=1}^{N_{\text{act}}}\left[\mathbb{C}(c)\,\underline{P}_k\ \text{sgn}(\tau_k^{\text{tr}})\ \frac{\Delta t}{\eta}(A_{kl})^{-1}\ \underline{P}_l^T\ \mathbb{C}(c)\ \text{sgn}(\tau_l^{\text{tr}})\right], \tag{33}$$

where the tangential stiffness $\underline{\mathbb{C}}^{\text{tan}}(c)$ is given by the derivative $\dfrac{\partial \underline{\boldsymbol{\sigma}}^{(n+1)}}{\partial \underline{\boldsymbol{\varepsilon}}^{(n+1)}}$.

4 Numerical Examples

The idealized model is implemented into a four-node quadrilateral plane element with bilinear shape functions. For all calculations, the elasticity tensors

$$\underline{\mathbb{C}}_{\text{fcc}} = \begin{bmatrix} 1.40 & 0.84 & 0.0 \\ 0.84 & 1.40 & 0.0 \\ 0.0 & 0.0 & 0.28 \end{bmatrix} 10^5\ \frac{\text{N}}{\text{mm}^2}, \qquad \underline{\mathbb{C}}_{\text{bcc}} = 1.1\,\underline{\mathbb{C}}_{\text{fcc}}, \tag{34}$$

are considered in Voigt notation, where the stiffness $\underline{\mathbb{C}}_{\text{fcc}}$ is taken from Yamanaka et al. (2008). Using Voigt notation, the eigenstrain is set to

$$\underline{\boldsymbol{\varepsilon}}^0(c) = \begin{bmatrix} c^2\varepsilon_{\text{vol}}^0 \\ c^2\varepsilon_{\text{vol}}^0 \\ c\,0.1 \end{bmatrix}, \tag{35}$$

where the volumentric entries $\varepsilon_{\text{vol}}^0 = 0$ unless otherwise specified. With $\varepsilon_{\text{vol}}^0 = 0$, the eigenstrain corresponds to a pure shear loading on the martensitic phase. The calibration constants are determined to be $\kappa_{\text{s}} = 2.4521$ and $\kappa_{\text{g}} = 2.1808$ so that $G = 0.1\frac{\text{J}}{\text{m}^2}$ is the interface energy density. This value lies within the range of the free energy densities of other phase field models, (see Schrade et al. (2009)). The parameter $L = 5$ nm is chosen sufficiently large, so that the transition zone can be resolved by several elements. Furthermore, the mobility constant $M = 1.0 \cdot 10^6\ \frac{\text{m}^3}{\text{Js}}$ is used. For all simulations, the microstructure evolution through the eigenstrain $\boldsymbol{\varepsilon}^0(c)$ is studied in the absence of external loads. Assuming an isothermal setting, the boundaries of the computation domain are stress free. In order to avoid rigid body movement, the bottom left corner is fixed in both the horizontal and the vertical directions; the bottom right corner is fixed in vertical direction. Furthermore, the following slip systems are taken into account

$$\boldsymbol{s}_1 = \boldsymbol{s}_3 = \begin{bmatrix} 1 \\ 0 \end{bmatrix}, \qquad \boldsymbol{n}_1 = \boldsymbol{n}_3 = \begin{bmatrix} 0 \\ 1 \end{bmatrix}, \qquad \Rightarrow \qquad \boldsymbol{P}_1 = \boldsymbol{P}_3 = \frac{1}{2}\begin{bmatrix} 0 & 1 \\ 1 & 0 \end{bmatrix}, \tag{36}$$

$$\boldsymbol{s}_2 = \boldsymbol{s}_4 = \frac{1}{\sqrt{2}}\begin{bmatrix} 1 \\ 1 \end{bmatrix}, \qquad \boldsymbol{n}_2 = \boldsymbol{n}_4 = \frac{1}{\sqrt{2}}\begin{bmatrix} -1 \\ 1 \end{bmatrix}, \qquad \Rightarrow \qquad \boldsymbol{P}_2 = \boldsymbol{P}_4 = \frac{1}{2}\begin{bmatrix} -1 & 0 \\ 0 & 1 \end{bmatrix}. \tag{37}$$

The slip systems $k = 1$ and $k = 3$ correspond to pure shear, i.e. compression and tension parallel to the diagonals of the quadratic computation domain. The slip systems $k = 2$ and $k = 4$ are associated with simple shear, i.e. compression parallel to the horizontal edges and tension parallel to the vertical edges of the quadratic specimen. The slip directions and the slip normals are depicted schematically in Fig. 4.

slip systems $k=1,3$ slip systems $k=2,4$

Figure 4: Slip normals and slip directions of the slip systems.

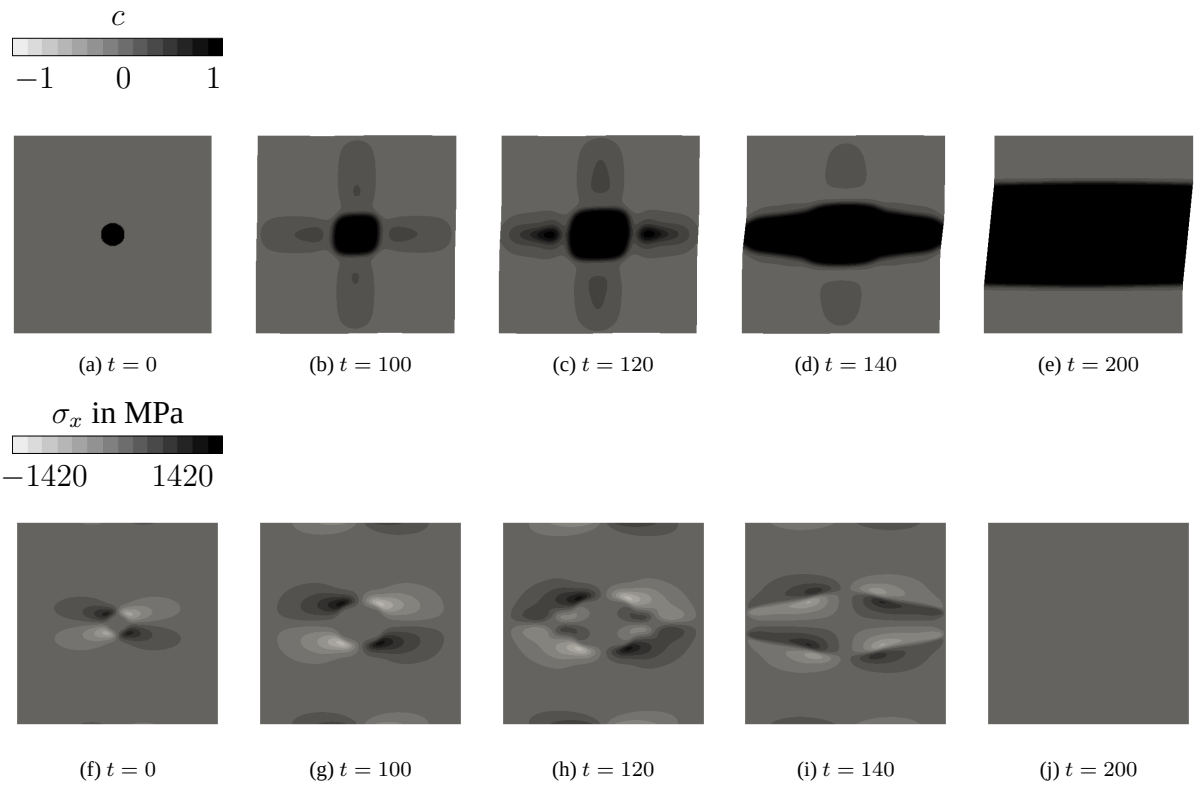

(a) $t=0$ (b) $t=100$ (c) $t=120$ (d) $t=140$ (e) $t=200$

(f) $t=0$ (g) $t=100$ (h) $t=120$ (i) $t=140$ (j) $t=200$

Figure 5: First row: evolution of the martensitic phase for a single circular nucleus (variant 1, black) in austenitic matrix (grey), elastic material behavior, deformed configuration.
Second row: normal strain component σ_x

4.1 Single Circular Martensitic Nucleus, Elastic Material

In a first example a single circular martensitic nucleus in an austenitic matrix is modeled with purely elastic material (no plasticity). This simple example does not feature complicated interactions so the results are comprehensible. The evolution of the martensitic phase can be seen in the first row of Figure 5, where the austenitic phase is depicted in grey ($c=0$) and the first martensitic orientation variant in black ($c=1$). Due to the initial configuration, for this example the second martensitic orientation variant does not appear. In Fig. 5 the transition zone is shown in order to illustrate its length scale compared to the specimen size. To present more complicated microstructures clearly, it is neglected in the following plots and the martensitic phase is shown for a value $c \geq 0.6$.

Figure 5(b) shows the martensitic nucleus growing without external load applied since martensite is the stable phase. Thus, the growing nucleus reduces the global separation energy $E^{\text{sep}} = \int_V \psi^{\text{sep}} \, \mathrm{d}V$. Initially, the martensitic phase grows in almost circular shape which leads to a small interface between the phases and is therefore favorable for the system as it results in a low contribution of the global gradient energy $E^{\text{grad}} = \int_V \psi^{\text{grad}} \, \mathrm{d}V$. After some time steps, however, due to the transformation induced eigenstrain $\boldsymbol{\varepsilon}^0(c)$, a martensitic plate is built (Figure 5(c)). The eigenstrain $\boldsymbol{\varepsilon}^0(c)$ induces shear stress on the martensitic nucleus with main shear directions in horizontal and vertical direction. This leads to a martensitic plate, which evolves either in horizontal or vertical

direction, depending on the exact initial position of the nucleus. In this case a plate in horizontal direction forms. When the plate has grown through the austenitic material, it widens in vertical directions until the matrix consists of exclusively martensitic material (Figure 5(e)), which yields the minimal global total energy $E^{\text{tot}} = \int_V \psi \, \mathrm{d}V$. The martensitic phase growing in a plate-like shape is confirmed by other theoretical studies, e.g. Yamanaka et al. (2008).

In the second row of Fig. 5, the normal stress component σ_x is plotted. For the initial configuration (Fig. 5(f)) it illustrates, that the stress induced by the eigenstrain within the martensitic nucleus decays in radial direction so that the boundaries are stress free. Hence, there is no influence of the boundary for the initial configuration. When the martensitic plate has grown through the matrix, the stress is considerably smaller (Fig. 5(j)). In this context, Fig. 5(e) shows that the stress is reduced due to a deformation of the specimen on the macroscale. Subsequently, in the following example the impact of the eigenstrain on the different slip systems is examined.

4.2 Single Circular Martensitic Nucleus, Elastoplastic Material

In the next example the single circular martensitic nucleus is studied again, now taking crystal plasticity into account. For the austenitic slip systems, the critical shear stress $\tau^{\text{cr}}_{\text{fcc}} = 200$ MPa is considered. The yield strength of the martensitic phase is about two to three times higher than that of the austenitic phase (Roumi (2010)), for this example the value of $\tau^{\text{cr}}_{\text{bcc}} = 450$ MPa is used. Figure 6 shows in the first column the evolution of the martensitic phase. Comparing Figure 6(f) with Figure 5(c), which both show the evolution of the martensitic phase for time step $t = 120$, reveals the martensitic plate growing slightly faster in purely elastic material. The plastic zone seems to constrain the martensitic transformation. This result is reasonable since the slip additionally dissipates **elastic** energy which is not available for the phase transition. Energetic considerations for this model are carried out in detail in Schmitt et al. (2013a,b).
Columns two to five of Figure 6 depict the norm of the slip for all slip systems; the first row refers to the initial configuration ($t = 0$). In Figure 6(b), it can be seen that the first slip system $k = 1$ is activated in the austenitic material around the nucleus, where the highest amount of slip can be seen in the directions rotated by 45° referring to the horizontal and vertical directions. It is an austenitic slip system which corresponds to a pure shear loading. This explains the formation of the plastic zone: Inside the nucleus, the eigenstrain acts as a pure shear loading with principal directions in 45°-directions. Since the nucleus is initially growing in circular direction, the amount of slip is higher in these areas. However, there is slip visible in horizontal and vertical directions around the nucleus, too. These are the main shear directions of the eigenstrain which lead to the plate propagating in horizontal direction. Therefore, the slip system $k = 1$ can be seen activated in horizontal and vertical directions in the following time steps. For time step $t = 140$, the martensitic plate has grown almost completely through the matrix. Figure 6(k) shows the slip system $k = 1$ additionally activated at the plate tips. This becomes intuitive, keeping the eigenstrain of the martensitic phase in mind, which corresponds to a pure shear loading. It leads to high resolved shear stresses in the austenitic material at the plate tips. For the vertically widening plate at time step $t = 200$, the plastic zones at the plate tips are slightly vertically elongated (Figure 6(q)). When the plate has grown completely through the austenitic domain, the system is able to reduce the elastic energy on the macro level through deformation so that the stresses are lower. Hence, the amount of the additional slip in system $k = 1$ in Figure 6(q) is very small.
The slip of the second austenitic system $k = 2$ is considerably higher than that of slip system $k = 1$. Figure 6(c) shows the slip system $k = 2$ activated in radial direction around then martensitic nucleus since the nucleus is initially growing in a circular shape. The strain direction associated with this slip system corresponds to a compression in horizontal direction and tension in vertical direction by the same amount, which explains the radial activation of slip system $k = 2$. As the plots show the norm of the slip, there is no distinction between expansion and compression visible. For the following time steps, the slip system $k = 2$ remains activated around the horizontally growing plate. Equally to slip system $k = 1$, there is slip at the plate tips, when the growing plate has almost reached the borders of the austenitic matrix (Figure 6(m)). For time step $t = 200$, there is no additional activation of slip in the system $k = 2$, however, a small part of the slip in Figure 6(r) is inherited by the martensitic phase: Figure 6(t) shows the slip system $k = 4$ activated at the vertical borders of the matrix, (where the material for that time step is martensitic). So the plastification of the austenitic slip system $k = 2$ proceeds in the martensitic slip system $k = 4$. Apart from that, the slip system $k = 4$ is not activated. The resolved shear stress of that slip system is below the critical shear stress $\tau^{\text{cr}}_{\text{bcc}}$.
The martensitic slip system $k = 3$ is activated within the nucleus, with the highest amount of slip in horizontal and vertical directions (Figure 6(d)), which is again due to the martensitic eigenstrain, acting as a pure shear loading with main shear directions in horizontal and vertical direction. After the first time step, the slip of the martensitic system $k = 3$ does not evolve further since the growing plate reduces the stresses within the nucleus (see column

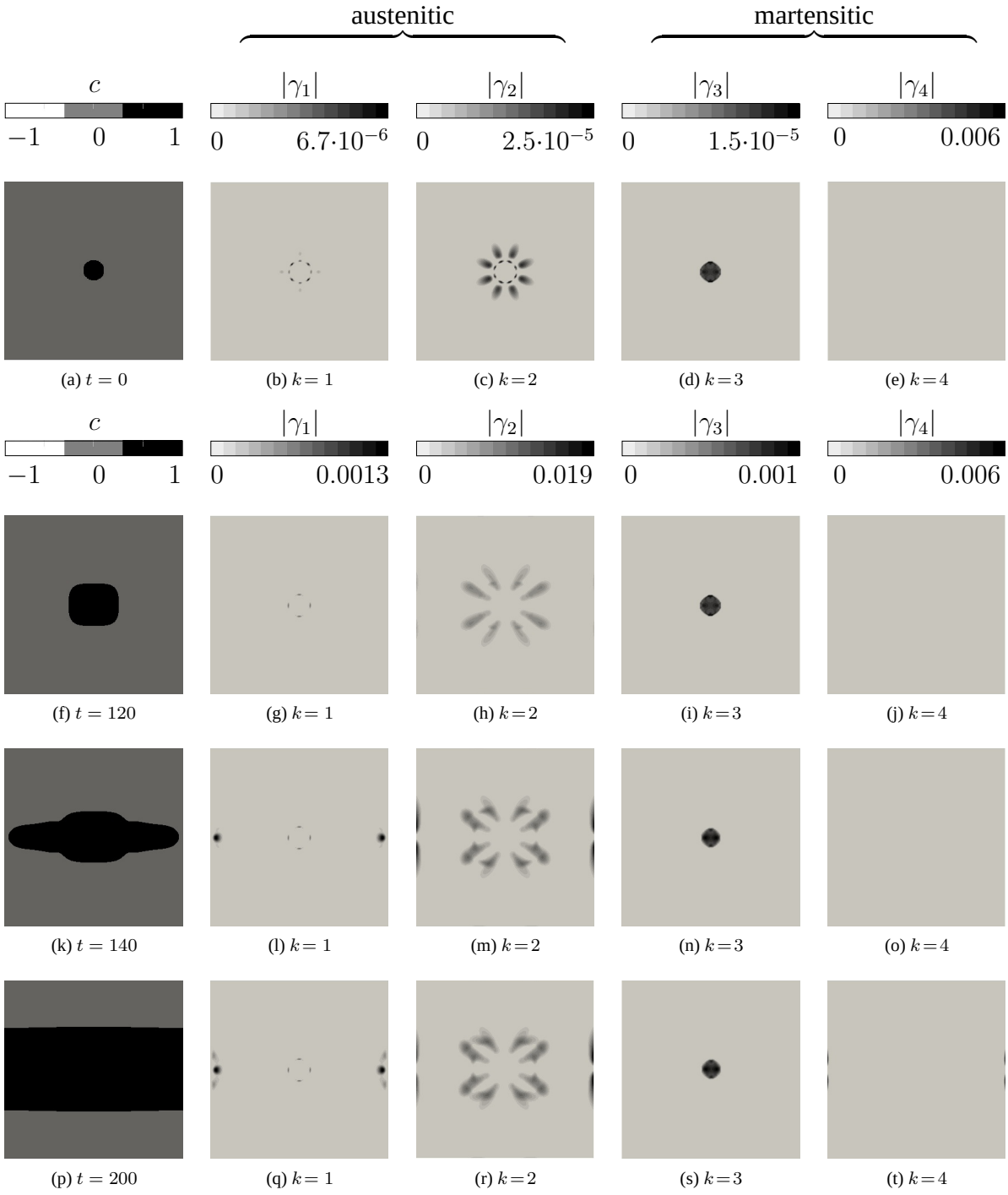

Figure 6: Single circular martensitic nucleus with $\varepsilon^0_{\text{vol}} = 0$.
Left: Martensitic evolution with crystal plasticity (variant 1: black, austenite: grey);
Right: Norm of the slip $|\gamma_k|$ for $k = 1, .., 4$.

four of Figure 6).
Hence, the results show strong interactions between the transformation induced eigenstrain in the martensitic phase and the behavior of the different slip systems while the slip constrains the evolution of the martensitic phase. Furthermore, the inheritance of slip from the austenitic to the martensitic phase can be observed. In a next step, the influence of a volumetric part of the transformation strain tensor $\boldsymbol{\varepsilon}^0$ on the activation of slip systems is considered.

4.3 Single Circular Martensitic Nucleus with Volumetric Eigenstrain, Elastoplastic Material

In this section, again a single circular martensitic nucleus is studied, taking crystal plasticity into account. However, here the volumetric eigenstrain in (35) is set to $\varepsilon^0_{\text{vol}} = 0.04$. Figure 7 shows in the first column the evolution of the martensitic phase. Employing the initial configuration of the previous examples, the volumetric part of the eigenstrain leads to a martensitic plate, growing in diagonal direction. This can be explained by considering the eigenstrain tensor $\boldsymbol{\varepsilon}^0(c)$ applied in this example: The pure shear part leads due to its main shear directions to a horizontally growing martensitic plate. The volumetric part of the eigenstrain tensor yields a nucleus growing in circular direction. The superposition of both parts results in the martensitic plate propagating in diagonal direction. The diagonal growing direction of the martensitic plate coincides with crystallographic theories of the martensitic transformation, e.g. Wechsler et al. (1953). For this example the diagonal direction is not preset by the nucleus but results from the volumetric part of the eigenstrain tensor $\boldsymbol{\varepsilon}^0(c)$. So evidently, the volumetric part of the the eigenstrain tensor $\boldsymbol{\varepsilon}^0(c)$ has to be taken into account for the modeling of martensitic transformations.
The first column of Figure 7, additionally depicts the evolution of the martensitic phase for a purely elastic material in white. At time step $t=10$, the difference is hardly visible (Figure 7(f)). Yet as in section 4.2, the following time steps show, that the slip constrains the growth of the martensitic plate since additional elastic energy is dissipated. Therefore, in Figures 7(k) and (p), the martensitic plate of the purely elastic material in white is larger than the martensitic phase depicted in black, where crystal plasticity is taken into account.
The impact of the volumetric part of the eigenstrain tensor $\boldsymbol{\varepsilon}^0(c)$ becomes evident, when considering the norm of the slip for the four slip systems (columns two to five in Figure 7). Generally, the additional volumetric part in the eigenstrain $\boldsymbol{\varepsilon}^0(c)$ yields higher stresses, so that the amount of slip in the austenitic slip systems is higher, compared to the example in Figure 6, where the same nucleus is studied with $\varepsilon^0_{\text{vol}} = 0$. Furthermore, all four slip systems are activated in a similar way compared to section 4.2. However, the slip system activation is rotated by 45° since the martensitic plate is growing in diagonal direction.
In the previous section 4.2 with $\varepsilon^0_{\text{vol}} = 0$, the slip system $k = 4$ is initially not activated (Figure 6(e)). With $\varepsilon^0_{\text{vol}} = 0.04$, the martensitic slip system $k=4$ shows a small amount of slip (Figure 7(e)) for the initial configuration. The strain direction associated with this slip system corresponds to a compression in horizontal direction and an expansion in vertical direction by the same amount with main shear directions in diagonal directions. Therefore, it is activated at the borders of the martensitic nucleus due to the volumetric part of the transformation strain in the martensitic phase. There is no additional activation of slip system $k=4$ in the following time steps as the stresses in the nucleus are reduced by the martensitic evolution.
Another observation concerns the austenitic slip system $k=2$. The initial configuration leads to ring-shaped slip of system $k=2$ around the nucleus (Figure 7(c)). For time step $t = 10$, Figure 7(h) shows within the ring of slip a small martensitic plate. This is depicted enlarged in Figure 8(a), indicating the martensitic phase in white. When the tip of the martensitic plate reaches the area of plasticity, the slip system $k = 2$ is activated at the sides of the plate tip (Figure 8(b), (c) and (d)). This leads to the two lines of plasticity in direction of the growing plate which can be seen for time steps $t = 100$ and $t = 150$ in Figure 7(m) and (r), respectively. The slip activated by the martensitic plate demonstrates the correlations between plasticity and the martensitic transformation.
Thus, the volumetric part of the eigenstrain tensor $\boldsymbol{\varepsilon}^0(c)$ leads to a martensitic plate growing rotated about 45° in diagonal direction which also results in a change in the areas of plastic slip. This influences the evolution of the martensitic phase. On the other hand, slip induced by the propagating martensitic plate is observed, too, which indicates strong interactions between plasticity and the martensitic tansformation. In the next section additionally the second martensitic orientation variant is studied, which differs in eigenstrain from the first variant.

4.4 Two Martensitic Nuclei with Volumetric Eigenstrain, Elastoplastic Material

The initial configuration applied for this section is depicted in Figure 9(a): an austenitic matrix with two circular nuclei, one of each orientation variant. As in section 4.3, crystal plasticity is considered and the volumetric part of the transformation strain is set to $\varepsilon^0_{\text{vol}} = 0.04$. Again, the first column of Figure 9 shows the evolution of the martensitic phase where the second martensitic orientation variant is illustrated in white. The nuclei can be seen growing in a plate-like shape in diagonal directions. Since the eigenstrain in (35) depends on the sign of the order

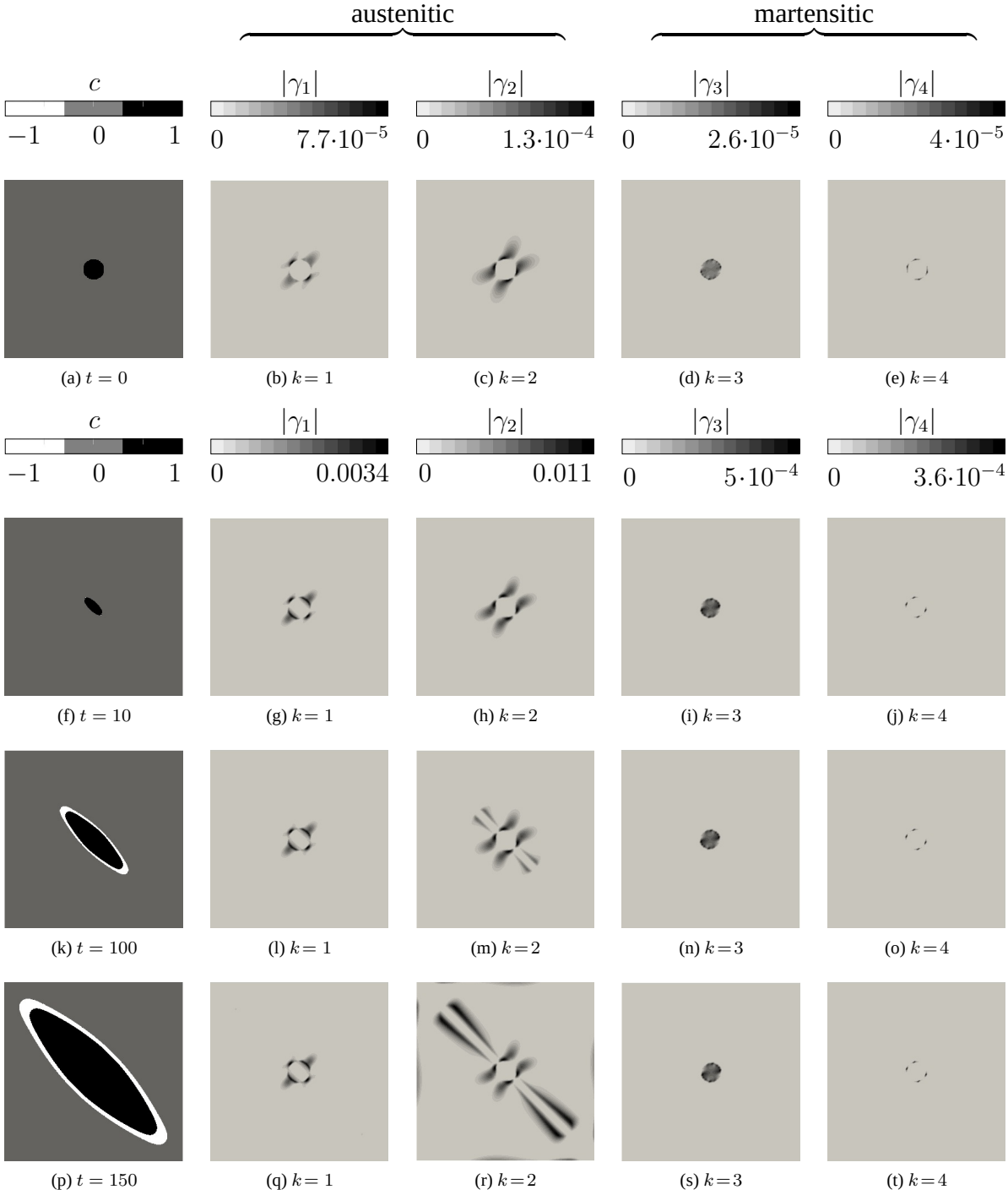

Figure 7: Single circular martensitic nucleus with $\varepsilon^0_{\text{vol}} = 0.04$.
Left: Martensitic evolution with crystal plasticity (variant 1: black, austenite: grey), elastic martensitic evolution white framed (for comparison); Right: Norm of the slip $|\gamma_k|$ for $k = 1, .., 4$.

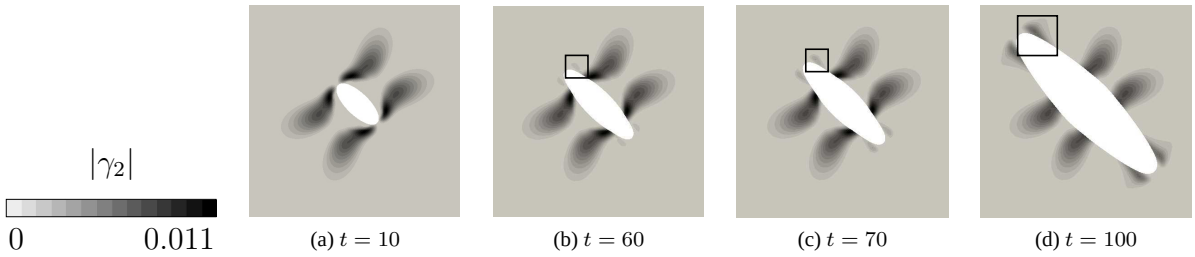

(a) $t = 10$ (b) $t = 60$ (c) $t = 70$ (d) $t = 100$

Figure 8: Norm of slip $|\gamma_2|$ for single circular martensitic nucleus (white) with $\varepsilon^0_{\text{vol}} = 0.04$, enlarged.

parameter c, the shear ε^0_{12} is positive for the first martensitic orientation variant ($c=1$) and negative for the second variant ($c=-1$). As a result, the different variant plates evolve perpendicular to each other. When the maximal extension in diagonal direction is reached, the plates start to widen, (Figure 9(u)). Analogously to the previous section, the martensitic evolution for purely elastic material is depicted as a white frame around the elasto-plastic plates which again indicates the elastic plate growing slightly faster. Thus, also for this example, the crystal plasticity affects the evolution of the martensitic phase since additional elastic energy is dissipated.
Furthermore, the amount of slip in the systems $k = 1, ..., 4$ is shown in columns two to five of Figure 9. The different signs of the transformation shear ε^0_{12} for the two variants lead to different areas of slip for the corresponding slip systems. Since the shear directions of the different variants are perpendicular to each other, the areas, where the slip systems are activated in response to each variant are perpendicular to each other, too. Apart from that, the observations of the previous section 4.3, can be found again in Figure 9: The martensitic slip system $k=4$ is activated due to the volumetric strain in the initial nuclei. Figure 9(e) shows the different directions of slip resulting from the different signs in transformation shear of the nuclei. The evolution of slip around the first nucleus is rotated by $90°$ referring to that of the second nucleus. Concerning the austenitic slip system $k=2$, the lines of plasticity induced by the martenitic plates evolve in both diagonal directions (Figure 9(r),(w)), in turn influencing the martensitic evolution: The elastic and the elasto-plastic martensitic plate do not only differ in size but also in shape, see Figure 9(p). At the left upper corner, the black elasto-plastic plate is sharper than the white frame of the elastic plate. In Figure 9(m) slip system $k=2$ is activated around plate tip, which constrains the widening of the martensitic phase. This is also observed at the tips of the variant two plate. Furthermore, the slip at the plate tips of the austenitic system $k=2$ is inherited by the corresponding martensitic slip system $k=4$ (Figure 9(t)).
In Figure 9(u) it can be seen, that the black martensitic variant one plate has almost reached the white plate of variant two. In the narrow austenitic area between the plates slip system $k=1$ is activated around the white variant two plate. The high resolved shear stress results from the transformation shear which acts in different directions within the appraoching plates.
For this section, it can be concluded, that the plates of the different orientation variants grow perpendicular to each other in diagonal direction, caused by the different signs in transformation shear in combination with the volumetric part of the transformation strain. Therefore, the slip in response of the different variants evolves perpendicular to each other, too. The general evolution of plasticity is plausible, indicating strong interactions between the slip and the martensitic transformation.

5 Conclusion

A phase field model for martensitic transformations considering crystal plasticity effects is introduced with the rate of the order parameter assumed to follow the time-dependent Ginzburg-Landau equation. Distinctive slip systems for the different phases are considered. The simulations show, that these are activated in a reasonable manner. In addition, the model is able to capture the inheritance of slip from one phase to another.
With aid of the model the interactions between the martensitic formation including the transformation induced eigenstrain and the plasticity of different slip systems are studied. Resorting to basic examples, the evolution of slip as a result of the transformation strain could be understood. The crystal plasticity is found to influence the formation of the martensitic phase since additional elastic energy is dissipated. On the other hand, slip induced by the martensitic transformation is observed, too. In this context, more realistic results are attained if not only transformation shear but also volumetric transformation strain are taken into account.
With the interactions understood, for future work more realistic examples will be considered. In this context, using a 3D model with a real crystallographic relations would enable the verification by experiments. Futhermore, it is assumed that slip comparable to the eigenstrains will lead to more realistic results. Another task is to include

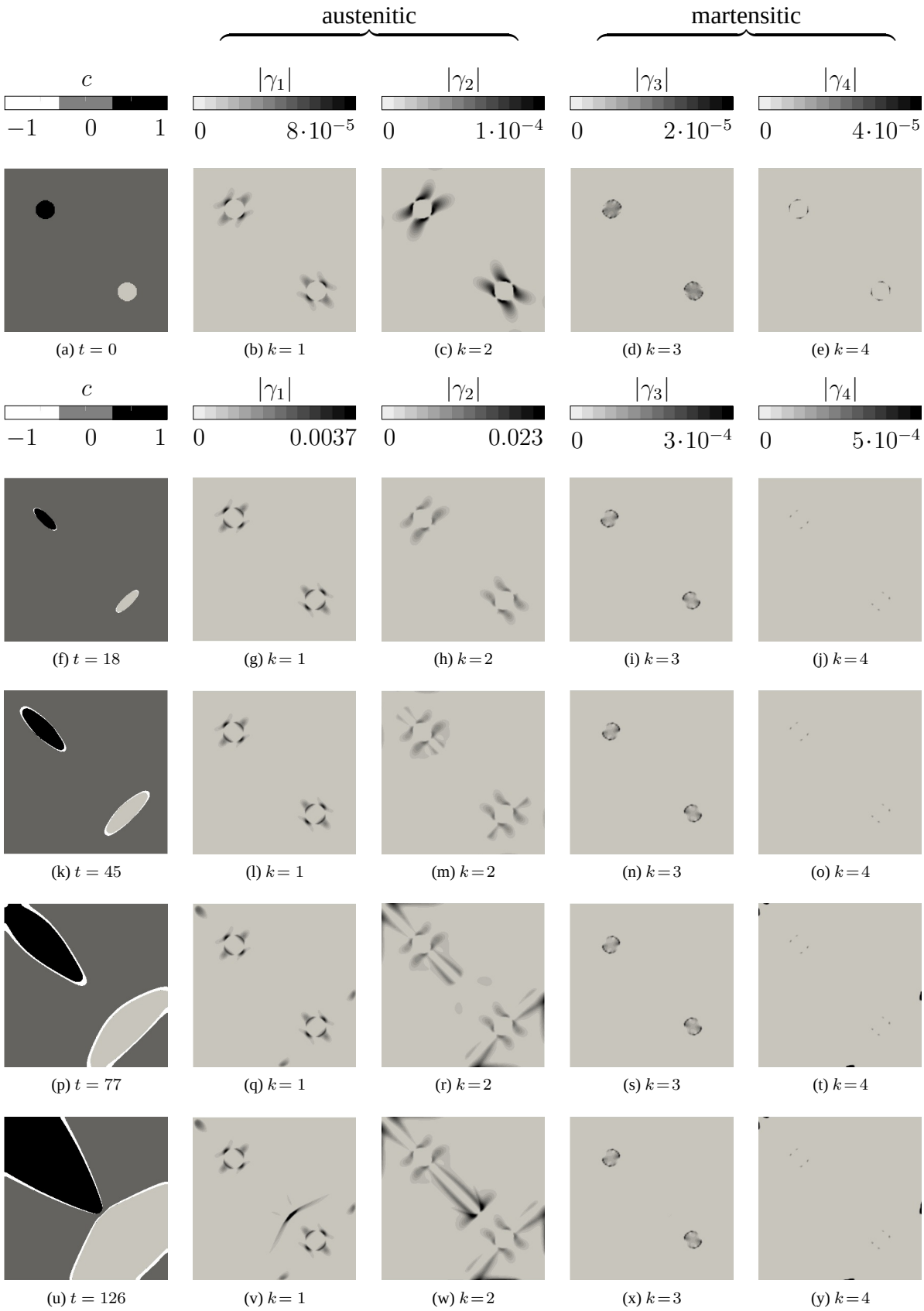

(a) $t=0$ (b) $k=1$ (c) $k=2$ (d) $k=3$ (e) $k=4$

(f) $t=18$ (g) $k=1$ (h) $k=2$ (i) $k=3$ (j) $k=4$

(k) $t=45$ (l) $k=1$ (m) $k=2$ (n) $k=3$ (o) $k=4$

(p) $t=77$ (q) $k=1$ (r) $k=2$ (s) $k=3$ (t) $k=4$

(u) $t=126$ (v) $k=1$ (w) $k=2$ (x) $k=3$ (y) $k=4$

Figure 9: Two circular martensitic nuclei with $\varepsilon^0_{\text{vol}} = 0.04$.
Left: Martensitic evolution with crystal plasticity (variant 1: black, variant 2: white, austenite: grey), elastic martensitic evolution white framed (for comparison); Right: Norm of the slip $|\gamma_k|$ for $k = 1, .., 4$.

additionally the interactions of phase transformations and plasticity through the kinetics.

6 Acknowledgments

This work was financially supported by the Deutsche Forschungsgemeinschaft, SFB 926.

References

Artemev, A.; Wang, Y.; Khachaturyan, A. G.: Three-dimensional phase field model and simulation of martensitic transformation in multilayer systems under applied stresses. *Acta Materialia*, 48, (2000), 2503–2518.

Bartel, T.; Hackl, K.: A novel approach to the modelling of single-crystalline materials undergoing martensitic phase-transformations. *Material Sience and Engineering A*, 481-482, (2008), 371–375.

Bartel, T.; Menzel, A.; Svendsen, B.: Thermodynamic and relaxation-based modelling of the interaction between martensitic phase transformations and plasticity. *Journal of Mechanics and Physics in Solids*, 59, (2011), 1004–1019.

Bhattacharya, K.: *Microstructure of martensite*. Oxford University Press (2003).

Cahn, J. W.; Hilliard, J. E.: Free energy of a nonuniform system. i. interfacial free energy. *The Journal of Chemical Physics*, 28, (1958), 258–267.

Chen, L.-Q.; Wang, Y.; Khachaturyan, A. G.: Kintetics of tweed and twin formation during an ordering transition in a substitutional solid solution. *Philosophical Magazine Letters*, 65, (1992), 15–23.

Cherkaoui, M.; Berveiller, M.: Micromechanical modeling of the martensitic transformation induced plasticity in steels. *Smart Mater. Struct.*, 9, (2000), 592–603.

Fischer, F. D.; Berveiller, M.; Tanaka, K.; Oberaigner, E. R.: Continuum mechanical aspects of phase transformations in solids. *Archive of Applied Mechanics*, 64, (1994), 54–85.

Hildebrand, F.; Miehe, C.: Variational phase field modeling of laminate deformation microstructure in finite gradient crystal plasticity. *Proceedings in Applied Mathematics and Mechanics*, 12, (2012), 37–40.

Hildebrand, F. E.; Miehe, C.: Comparison of two bulk energy approaches for the phasefield modeling of two-variant martensitic laminate microstructure. *Technische Mechanik*, 32, (2011), 3–20.

Jin, Y. M.; Artemev, A.; Khachaturyan, A. G.: Three-dimensional phase field model of low-symmetry martensitic transformation in polycrystal: simulation of ζ_2'-martensite in aucd alloys. *Acta Materialia*, 49, (2001), 2309–2320.

Kundin, A.; Raabe, D.; Emmerich, H.: A phase-field model for incoherent martensitic transformations including plastic accomodation process in the austenite. *Journal of Mechanics and Physics in Solids*, 59, (2011), 2082–2102.

Levitas, V. I.; Lee, D.-W.; Preston, D. L.: Interface propagation and microstructure evolution in phase field models of stress-induced martensitic phase transformations. *International Journal of Plasticity*, 26, (2009), 395–422.

Olson, G. B.; Cohen, M.: Kinetics of strain-induced martensitic nucleation. *Metallurgical and Materials Transactions A*, 6A, (1975), 791–795.

Richards, A. W.; Lebensohn, R. A.; Bhattacharya, K.: Interplay of martensitic phase transformation and plastic slip in polycrystal. *Acta Materialia*, 61, (2013), 4384–4397.

Roumi, F.: *Shape Changing Transformations: Interactions with Plasticity and Electrochemical Processes*. Ph.D. thesis, California Institute of Technology, Pasadena, California (2010).

Schmitt, R.; Müller, R.; Kuhn, C.; Urbassek, H. M.: A phase field approach for multivariant martensitic transformations of stable and metastable phases. *Archive of Applied Mechanics*, 83, (2013a), 849–859.

Schmitt, R.; Müller, R.; Skorupski, R.; Smaga, M.; Eifler, D.: A phase field appraoch for martensitic transformations in elastoplastic materials. *Proc. Appl. Math. Mech.*, 13, (2013b), 213–214.

Schmitt, R.; Wang, B.; Urbassek, H. M.; Müller, R.: Modeling of martensitic transformations in pure iron by a phase field approach using information from atomistic simulation. *Technische Mechanik*, 33, (2013c), 119–130.

Schrade, D.; Mueller, R.; Xu, B.; Gross, D.: Domain evolution in ferroelectric materials: a continuum phase field model and finite element implementation. *Computer methods in applied mechanics and engineering*, 196, (2007), 4365–4374.

Schrade, D.; Müller, R.; Gross, D.: Parameter identification in phase field models for ferroelectrics. *Proc. Appl. Math. Mech.*, 9, (2009), 369–370.

Schrade, D.; Müller, R.; Gross, D.: On the physical interpretation of material parameters in phase field models for ferroelectrics. *Archive of Applied Mechanics*, 83, (2013), 1393–1413.

Schrade, D.; Xu, B. X.; Müller, R.; Gross, D.: On phase field modeling of ferroelectrics: parameter identification and verification. *SMASIS*, 1, (2008), 299–306.

Schröder, J.; Miehe, C.: Aspects of computational rate-independent crystal plasticity. *Computational Material Science*, 9, (1997), 168–176.

Skorupski, R.; Smaga, M.; Eifler, D.; Mayer, P.; Aurich, J. C.: Low cycle fatigue behavior of aisi 347 with varied surface morphology. *Proc. LCF7*, 7, (2013a), 39–44.

Skorupski, R.; Smaga, M.; Eifler, D.; Mayer, P.; Aurich, J. C.: Phase transformation as a result of mechanical loading and turning of metastable austenitic steels. *TMS2013 Proc.*, pages 877–884.

Wang, Y.; Khachaturyan, A. G.: Three-dimensional field model and computer modeling of martensitic transformations. *Acta Materialia*, 2, (1997), 759–773.

Wechsler, M. S.; Lieberman, D. S.; Read, T. A.: On the theory of the formation of martensite. *Journal of Metals*, November, (1953), 1503–1515.

Yamanaka, A.; Takaki, T.; Tomita, Y.: Elastoplastic phase-field simulation of self- and plastic accommodations in cubic → tetragonal martensitic transformation. *Material Sience and Engineering A*, 491, (2008), 378–384.

Yamanaka, A.; Takaki, T.; Tomita, Y.; Yoshino, M.: Crystal plasticity phase-field simulation of deformation behavior and microstructure evolution in polycrystalline material. In: E. Oate; D. R. J. Owen, eds., *X International Conference on Computional Plasticity* (2009).

Address: R. Schmitt, Institute of Applied Mechanics, University of Kaiserslautern, Gottlieb-Daimler-Straße, D-67663 Kaiserslautern
C. Kuhn, Institute of Applied Mechanics, University of Kaiserslautern, Gottlieb-Daimler-Straße, D-67663 Kaiserslautern
R. Müller, Institute of Applied Mechanics, University of Kaiserslautern, Gottlieb-Daimler-Straße, D-67663 Kaiserslautern
K. Bhattacharya, Division of Engineering and Applied Science, California Institute of Technology, Pasadena, CA 91125, USA
email: rschmitt@rhrk.uni-kl.de